JJEE
Volume 11 | Number 3 | September 2025 | Pages 546-564

Jordan Journal of Electrical Engineering

ISSN (print): 2409-9600, ISSN (online): 2409-9619

Homepage: jjee.ttu.edu.jo

Faulty Section Identification in Medium-Voltage Distribution Networks by Time-Frequency Feature Fusion of Transient Zero-Mode Current

Wangqing Mao[1*], Xiuru Wang[2], Jian Sun[3], Hangyu Zhao[4], Rao Fu[5], Mengmeng Cao[6]

[1] School of Automation Science and Engineering, Xi'an Jiaotong University, Xi'an, China
Email: 4522254003@stu.xjtu.edu.cn
[2, 4, 6] Suqian Power Supply Branch, State Grid Jiangsu Electric Power Co., Ltd., Suqian, China
[3] State Grid Jiangsu Electric Power Co., Ltd. Electric Power Research Institute, Nanjing, China
[5] Jilin Power Supply Branch, State Grid Jilin Electric Power Co., Ltd., Jilin, China

Received: Apr 10, 2025 *Revised: Jun 22, 2025* *Accepted: Sep 02, 2025* *Available online: Nov 27, 2025*

***Abstract*—** The accuracy of fault section identification using a single criterion is compromised under certain complex fault conditions, particularly when a single-phase grounding fault occurs in a neutral point ungrounded system, where the steady-state fault signal is weak. This paper addresses this challenge by investigating the distribution feature of zero-mode current in such systems and proposes three distinct methods for locating single-phase ground faults: the transient power method, characteristic frequency method, and transient current similarity method. Each method has its own strengths and can complement each other. Hence, fuzzy theory is utilized to establish membership functions and weight coefficients for the three methods, respectively. The weighted coefficient method is then employed to integrate the three criteria, eliminating issues such as blind areas and misjudgments in fault section identification resulting from relying solely on a single criterion. A simulation model is developed using PSCAD/EMTDC. The results obtained under various fault conditions confirm the effectiveness and robustness of the fusion method in accurately identifying fault sections.

***Keywords*—** Transient feature; Transient power; Characteristic frequency; Waveform similarity; Fault section identification; Fuzzy theory.

1. INTRODUCTION

As power systems progress, the distribution network has significantly expanded, leading to increased emphasis on its power supply reliability and stable operation [1, 2]. Failure to address a single-phase ground fault can escalate into more serious short-circuit faults, presenting a substantial risk to the system's safety and significantly reducing the lifespan of power equipment [3, 4].

The fault section identification techniques can be broadly categorized into digital quantity-based and electric quantity-based methods [5, 6]. Within digital quantity-based techniques, there are two subcategories: graph theory-based and artificial intelligence (AI)-based methods, each operating on different principles [7–9]. The graph theory-based method begins by outlining the distribution network's topology using the network description matrix. It then gathers current and voltage data from the feeder terminal to create the corresponding fault information matrix. Subsequently, utilizing the principles of graph theory, the method calculates these matrices to generate the fault judgment matrix [10]. AI-based methods can be further divided into two main categories [11, 12]. One is to combine the topology of the power

* Corresponding author
DOI: https://doi.org/10.5455/jjee.204-1744298232

grid to construct a switching function. By solving an objective function using optimization algorithms, the optimal value is determined to locate the fault [13]. The second method makes use of features like variations in electrical quantities that occur during a failure event. Both conventional machine learning methods and deep learning algorithms are used to turn this data into a classification issue [14].

On the other hand, electric quantity-based methods extract fault features and set threshold criteria by means of different signal processing techniques to achieve fault location [15]. They can be further categorized into active and passive methods [16, 17]. Passive methods extract the features of the fault signal to locate the section [18].

Conversely, active techniques introduce a particular frequency signal into the power system and identify the fault segment by analyzing the distribution of the injected signal's flow direction in the line [19].

The neutral point ungrounded mode is commonly used in distribution networks due to its low fault currents during single-phase grounding and high-power supply reliability. However, traditional steady-state methods face difficulties in ungrounded systems due to capacitive coupling effects and weak fault signatures. Distinguishing fault line characteristics from non-fault line characteristics during a single-phase ground fault remains a challenging task. This difficulty impedes fault line selection and section localization. \

Moreover, various interference factors introduce significant fuzziness and uncertainty in fault characteristic parameters [20]. Consequently, relying on a single criterion to ensure effective ground fault section location under different operating modes, line configurations, and fault types is challenging.

The transient electrical quantities of faults exhibit more obvious characteristics than the steady-state quantities, rendering them particularly suitable for fault analysis in ungrounded systems [16]. This research presents a new method for identifying faulty lines in power distribution systems by utilizing transient electrical properties as fault characteristics. The main contributions are as follows:

(1) Novel Application Context and Innovative Feature Combination: We developed the comprehensive framework applying multi-feature fusion specifically for fault section identification in neutral point ungrounded distribution systems. Our work is the first to integrate: Hilbert transform-based transient power analysis, S-transform characteristic frequency detection and Waveform similarity correlation in a unified fuzzy decision framework for this application.

(2) Adaptive Weighting Mechanism: We introduced dynamic weight adjustment in the fusion process based on real-time fault characteristics, overcoming limitations of static fusion approaches.

(3) Implementation Effect: The method is less affected by error data compared to existing techniques while maintaining high accuracy under challenging conditions (high impedance faults up to 1000 Ω).

Sections 2 to 4, the distribution characteristics of transient zero-mode components are analyzed, and three fault section identification criteria are constructed. Section 5 presents the multi-transient feature fusion framework and puts forth a fault identification approach based on fuzzy decision making.

The simulation results and comparative studies are shown in Section 6. Finally, the article concludes with a summary in Section 7.

2. TRANSIENT POWER METHOD

After the unground distribution system has a single-phase ground fault, the zero-mode network is shown in Fig. 1. T represents the transformer. C_{01} and C_{02} represent the equivalent ground capacitances of line 1 and line 2, with the fault point F situated on line 3. Points A, B, and C along the line are sectional switches. The final point on the line is D. The ground capacitances of sections AB, BF, FC, and CD are C_{f1}, C_{f2}, C_{f3}, and C_{f4}, respectively. Both the zero-mode current upstream and downstream of the fault location are represented by $i_{0l} = i_{Cf3} + i_{Cf4}$ and $i_{0l} = i_{Cf3} + i_{Cf4}$. The measurement reference direction of the current is represented by dotted arrows, while the flow direction of the current is represented by blue solid arrows.

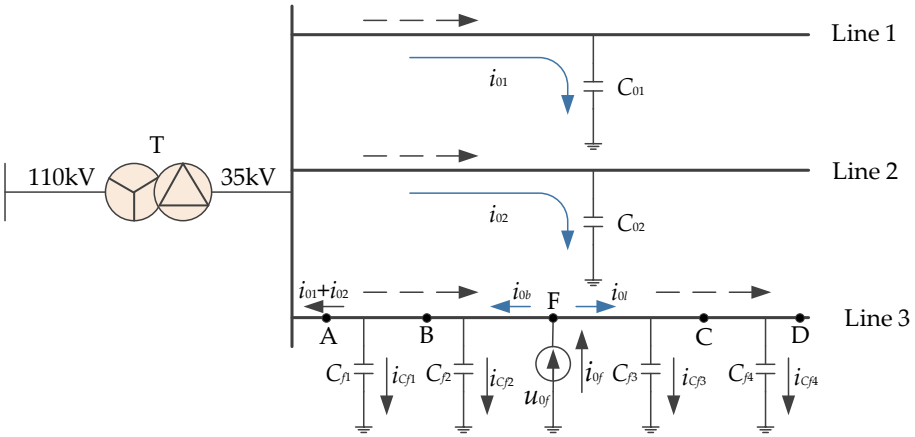

Fig. 1. The ungrounded distribution system's zero-mode network post-fault.

The current at the local terminal measurement point of the healthy line is the capacitance current that flows via the ground between the bus and the load. This current flows from the measurement point towards the end of the line. Similarly, the current that flows in the line downstream of the fault location is the capacitance current of the line to ground between the measurement point and the load, moving from the fault point towards the load. The current at the upstream measurement point of the faulty line is the sum of the ground capacitance current of the line between the measurement site and the busbar, as well as the ground capacitance current of all healthy lines. It is important to mention that the direction of the current in the healthy line and the line downstream of the fault point are same, while the polarity of the current two sides of the fault point is opposite.

Figure 2 depicts the fault equivalent circuit, which is composed of zero-mode, aerial-mode (include 1-mode and 2-mode) networks. R_1 and L_1 are the 1-mode network's resistance and inductance. The 2-mode network parameters are the same as those of 1-mode. The resistance, inductance, and capacitance of the zero-mode network are R_0, L_0, and C_0, respectively. U_f represents the virtual equivalent power supply. The zero-mode, 1-mode, and 2-mode voltages are U_{0f}, U_{1f}, and U_{2f}, and R_f is the fault resistance.

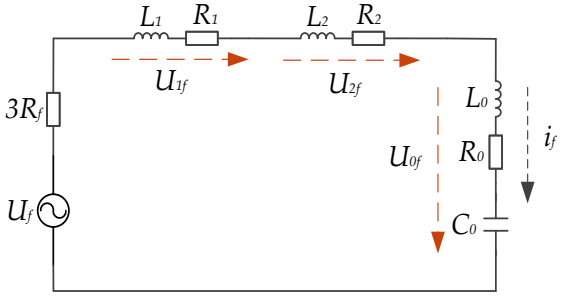

Fig. 2. Fault transient equivalent circuit of neutral point ungrounded system.

Let $L = L_1 + L_2 + L_0$, $R = R_1 + R_2 + R_0 + 3R_f$, $U_f(t) = U_m sin(\omega_0 t + f)$, the circuit equation can be written based on Fig. 2 as:

$$Ri_f + L\frac{di_f}{dt} + \frac{1}{C_0}\int_0^t i_f dt = U_f \tag{1}$$

By solving the equation, we can obtain the transient zero-mode current as Eq. (2).

$$\begin{cases} i_f(t) = U_m \omega_0 C\left[\dfrac{\omega_f}{\omega_0} sinfsin\omega_f t - cosfcos\omega_f t\right] e^{-\delta t} \\ \omega_f = \sqrt{\dfrac{1}{LC} - \left(\dfrac{R}{2L}\right)^2}, \ \delta = R/(2L) \end{cases} \tag{2}$$

where ω_f denotes the main resonant frequency, δ is the attenuation coefficient. The transient aerial mode voltage satisfies:

$$u_{1f} = u_{2f} = L_1\frac{di_f}{dt} + R_1 i_f = (R_1 - L_1\delta) i_f + i_f \omega_f U_m \omega_0 C\left[\frac{\omega_f}{\omega_0} sinfcos\omega_f t + cosfsin\omega_f t\right] e^{-\delta t} \tag{3}$$

Since $\left|(R_1 - L_1\delta)/\omega_0\right| = L_1$ and $\left|R_1 - L_1\delta\right| = L_1\omega_f{}^2/\omega_0$, the value of $(R_1 - L_1\delta) i_f$ is small and can be ignored. A clear phase relationship may be seen when comparing the aerial-mode voltage and zero-mode current:

(1) The zero-mode current's direction at each measurement points of both the fault lines downstream and non-fault lines remain consistent, and the current flows toward the line's end.

(2) The aerial-mode voltage is 90° ahead of the zero-mode current.

There are multiple resonant components in the actual transient process, arising from the series connection of zero-mode and aerial-mode networks in the equivalent circuit. As a result, the frequency components of the aerial-mode voltage are 90° ahead of the corresponding frequency's zero-mode current.

Conversely, the frequency components of the transient aerial-mode voltage lag behind the corresponding frequency component of the zero-mode current by 90° for zero-mode current upstream of the fault location.

The relationship between transient line voltage and transient aerial-mode voltage is obtained according to Kalenbauer transform (considering an A-phase ground fault as an example):

$$\begin{cases} u_{ab} = u_a - u_b = 3u_{1f} \\ u_{ac} = u_a - u_c = 3u_{2f} \end{cases} \tag{4}$$

where u_{ab} and u_{ac} represent the line voltage, u_a, u_b, and u_c are the three-phase phase-voltage. Assuming a line voltage phase shift of -90°, the zero-sequence current from the fault point to the bus will lead the line voltage by 180°, while the zero-sequence current downstream of the non-fault line and the fault line will be in phase with the line voltage.

The Hilbert transform for a continuous time signal is thus introduced. The Hilbert transform is defined as:

$$x(t) = \frac{1}{\pi}\int_{-\infty}^{+\infty}\frac{x(\tau)}{t-\tau}d\tau = \frac{1}{\pi}\int_{-\infty}^{+\infty}\frac{x(t-\tau)}{\tau}d\tau = x(t) * \frac{1}{\pi t} \tag{5}$$

It is possible to think of $x(t)$ as the result of the signal $x(t)$ that has been passed through a filter, with $h(t) = 1/\pi t$ representing the filter's unit impulse response. According to Fourier

transform theory, $jh(t)=j/\pi t$ is the result of Fourier transform and $sgn(\Omega)$ is the sign function. The frequency response of the Hilbert transformer is:

$$H(j\Omega)=-jsgn(\Omega)=\begin{cases}-j & \Omega>0\\ j & \Omega<0\end{cases} \tag{6}$$

If $H(j\Omega)=|H(j\Omega)|e^{j\varphi(\Omega)}$, then $|H(j\Omega)|=1$, and

$$\varphi(\Omega)=\begin{cases}-\pi/2 & \Omega>0\\ \pi/2 & \Omega<0\end{cases} \tag{7}$$

That is, the characteristics of this Hilbert transformer are as follows: The positive frequency signal is phase-shifted by -90°, the negative frequency signal is phase-shifted by +90°, and the amplitude-frequency characteristic is 1. The transient line voltage signal corresponding to the fault has the following Hilbert transform:

$$u(t)=\frac{1}{\pi}\int_{-\infty}^{+\infty}\frac{u(\tau)}{t-\tau}d\tau=u(t)*\frac{1}{\pi t} \tag{8}$$

Defined the transient power direction parameter (Q) as the mean value of the line voltage multiplied by the zero-mode current after undergoing Hilbert transformation, during a specified time period (T).

$$Q=\frac{1}{T}\int_0^T i(t)u(t)dt \tag{9}$$

Figsure 3 is the diagram of transient line voltage $u(t)$ and its corresponding Hilbert transform $u(t)$.

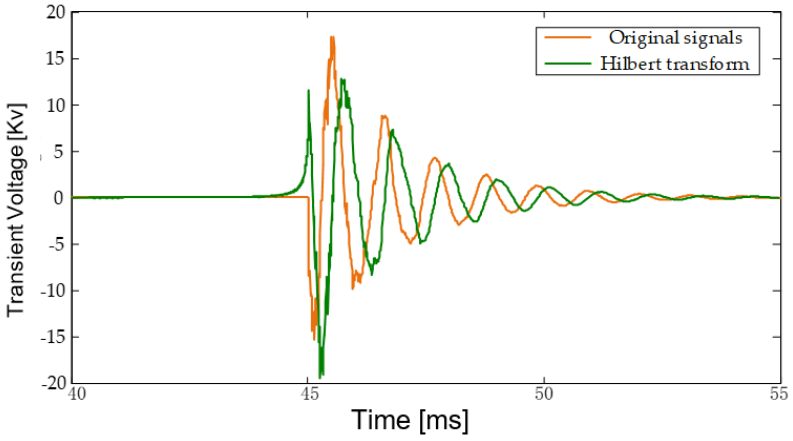

Fig. 3. Transient line voltage and its Hilbert transform waveform.

It can be observed from Fig. 3 that the transient line voltage is consistent with the polarity of the transient current after Hilbert transformation. Consequently, in this scenario, the transient power direction parameter Q>0. In the region upstream of the fault towards the busbar, the transient line voltage lags the zero-sequence current by 90° and the transient power direction parameter Q is negative.

3. CHARACTERISTIC FREQUENCY METHOD

Different equivalent zero-mode network parameters exist both upstream and downstream of the fault spot, as seen in Fig. 1. As a result, when there is series resonance in the zero-mode network, the transient current's main resonant frequencies are different upstream and downstream of the fault point. However, the main resonant frequency of the

zero-mode current does not vary much across two neighboring measurement sites on the same side of the fault location. The transient zero-mode current's frequency components of different measuring points are displayed in Fig. 4. Thus, the portion containing the fault can be identified via comparing the main resonant frequencies of the zero-mode current at nearby measurement sites. This method needs only transient zero-mode current data. The amount of data uploaded by this method is small, the requirements for communication and time synchronization are not high and proves to be convenient and dependable.

The S transform has excellent abilities for time-frequency positioning and resolution. It includes results for signal feature extraction that are easy to understand in addition to reflecting the local peculiarities of non-stationary signals [21].

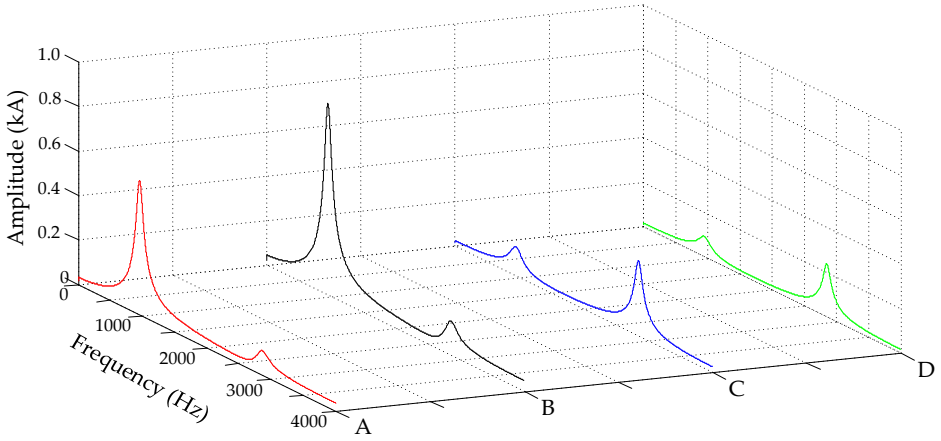

Fig. 4. The zero-mode current's frequency component at different measurement points.

In order to determine the main resonant frequency, the S transform is selected. A continuous S transform is performed on the signal $h(t)$:

$$\begin{cases} S(\tau,f)=\int_{-\infty}^{+\infty}h(t)\omega(\tau-t,f)e^{-j2\pi ft}dt \\ \omega(\tau-t,f)=\dfrac{|f|}{\sqrt{2\pi}}exp\left(\dfrac{-f^2(\tau-t)^2}{2}\right) \end{cases} \tag{10}$$

where $\omega(\tau-t,f)$ represents the window function, and τ is used to control the time window's location on the time axis, the frequency is *f*, and the imaginary unit is *j*. The inverse transformation formula of the S transform is:

$$h(t)=\int_{-\infty}^{+\infty}\left[\int_{-\infty}^{+\infty}S(\tau,f)d\tau\right]e^{j2\pi ft}df \tag{11}$$

The S-transform can be obtained by defining the mother wavelet as the product of the window function and the complex vector, then replacing it in the specification of the continuous wavelet. The phase correction in the continuous wavelet transform can be conceptualized as the S-transform. S transform's connection to its Fourier transform is as follows:

$$S(\tau,f)=\int_{-\infty}^{+\infty}H(\alpha+f)e^{-\frac{2\pi^2\alpha^2}{f^2}}e^{j2\pi\alpha\tau}d\alpha \tag{12}$$

The discrete S transform is obtained as follows: The discrete time sequence is recorded as $h(kT)$, with T serving as the sample time interval. The discrete Fourier transform of this series is:

$$H\left(\frac{n}{NT}\right)=\frac{1}{N}\sum_{K=0}^{N-1}h(kT)e^{-j\frac{2\pi nk}{N}} \tag{13}$$

Let $f = n/NT$, $\tau = iT$, the discrete S-transformation is:

$$S\left(iT, \frac{n}{NT}\right) = \sum_{m=0}^{N-1} H\left(\frac{m+n}{NT}\right) e^{-j\frac{2\pi^2 m^2}{n^2}} e^{j\frac{2\pi mi}{N}}, n \neq 0 \tag{14}$$

The inverse transformation is expressed by Eq. (15).

$$h(kT) = \sum_{K=0}^{N-1} \left\{ \frac{1}{N} \sum_{j=0}^{N-1} S\left[jT, \frac{n}{NT}\right] \right\} e^{j\frac{2\pi nk}{N}} \tag{15}$$

A complex time-frequency matrix is the output of the S-transform on discrete time series, while the modular time-frequency matrix is produced by modulo operation. Various frequency components' amplitudes at a given instant are represented by the column vectors of the modulo time-frequency matrix, while the relationship between the amplitude of a certain frequency component changing with time is shown by the row vectors.

To verify the amplitude-frequency representation ability of S transform on mutation signals, take the signal as defined in Eq. (16), with a sampling frequency is 256 Hz.

$$\begin{cases} h[0:40] = cos(20\pi t) \\ h[41:50] = cos(20\pi t) + cos(200\pi t) \\ h[51:100] = cos(20\pi t) \\ h[101:180] = cos(100\pi t) \\ h[181:256] = cos(180\pi t) \end{cases} \tag{16}$$

The signal waveform is shown in Fig. 5. S-transform is performed on the signal to obtain the amplitude-frequency characteristic pseudo-color map as Fig. 6.

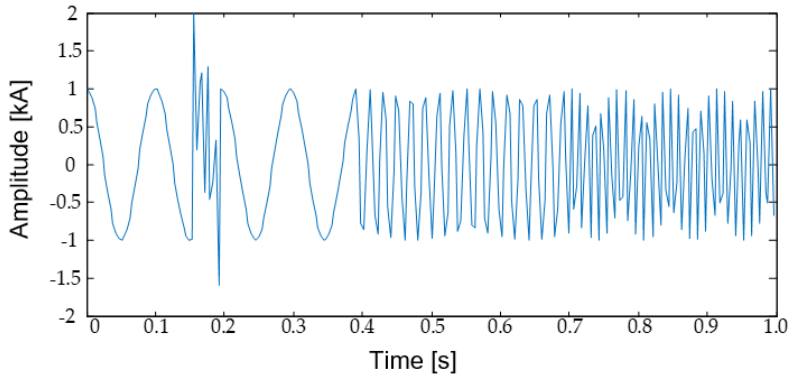

Fig. 5. Transient zero-mode current waveform.

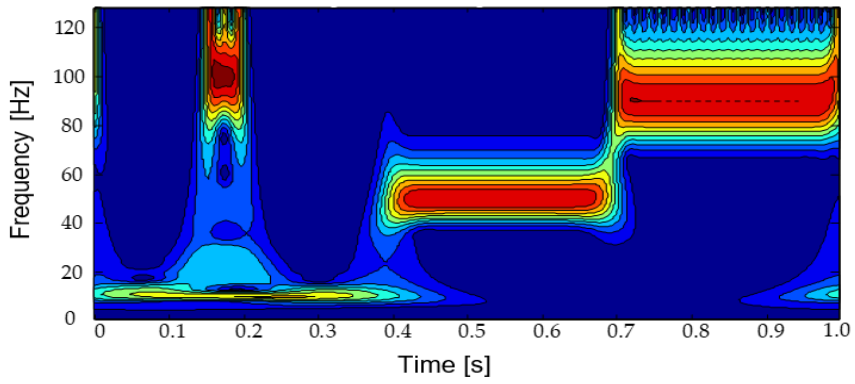

Fig. 6. Amplitude-frequency characteristic pseudo-color image after *S* transform.

As depicted in Fig. 6, the S transform can analyze the amplitude-frequency distribution characteristics of the signal in each time period. It has higher frequency resolution and lower time resolution for low-frequency components, while the opposite is true for high-frequency components.

4. TRANSIENT CURRENT SIMILARITY METHOD

Figure 1 shows that the upstream and downstream networks' transient processes can be regarded as independent of one another. The network characteristics for each side determine the zero-mode currents, and the transient currents' polarity is opposite on both sides. Two adjacent measurement points on the same side of the fault location have similar current frequencies and amplitudes, as well as highly similar waveforms. On the other hand, the two sites on different sides of the fault measure different current waveforms. Therefore, the defective part can be found using the waveform similarity of adjacent measurement points. The correlation coefficient is used to quantify the similarity between two signals (after discrete sampling):

$$\rho = \frac{\sum_{n=1}^{N} i_{01}(n) i_{02}(n)}{\sqrt{\sum_{n=1}^{N} {i_{01}}^2(n) \sum_{n=1}^{N} {i_{02}}^2(n)}} \tag{17}$$

where the sampling sequence is n, and the signal length is N, $i_{01}(n)$ and $i_{02}(n)$ are two zero-mode currents.

In the non-fault section, the transient current waveforms measured on both sides demonstrate a high degree of similarity, with a correlation coefficient close to 1. Conversely, within the faulted section, the resemblance between the transient current signals obtained from the upstream and downstream measurement points is low, and the correlation coefficient is much less than 1.

In actual engineering scenarios, each measurement point may not be accurately calibrated. and mathematical methods can be used to reduce the impact of signal out-of-synchronization on the similarity calculation results. One approach is to use one signal as a reference and to get the correlation coefficient at each shift by translating the other signal back and forth.

The optimal alignment is shown by the correlation coefficient that is the highest. When the signals are similar, the correlation coefficient from the point with the optimal overlap is the highest, indicating approximate synchronization. Conversely, for dissimilar signals, even after translation maximizes the correlation coefficient, the value remains very low (approaching zero). The following procedures are used to determine the zero-mode current's maximum coefficient at adjacent points:

(1) The timing error time is Δt (usually about 1~3 ms), and the maximum number of points that the signal can move forward and backward is $k_0 = \Delta t * f$, where f is the sampling frequency.

(2) Determine the number of translation points that correspond to the highest correlation coefficient value within the range of forward and backward translation:

$$\left|\sum_{k=1}^{K} i_{0m}(k - k_0') i_{0n}(k)\right| = max\begin{pmatrix} \left|\sum_{k=1}^{K} i_{0m}(k - k_0) i_{0n}(k)\right| \\ \left|\sum_{k=1}^{K} i_{0m}(k - k_0 + 1) i_{0n}(k)\right| \\ \cdots \\ \left|\sum_{k=1}^{K} i_{0m}(k + k_0) i_{0n}(k)\right| \end{pmatrix} \tag{18}$$

where m and n represent the measurement point number, the two transient current signals are i_{0m} and i_{0n}, and the signal length is K.

(3) The maximum correlation coefficient of two current is:

$$\rho_{max}\left(i_{0m},i_{0n}\right)=\frac{\left|\sum_{k=1}^{K} i_{0m}\left(k-k_0'\right)i_{0n}\left(k\right)\right|}{\sqrt{\sum_{k=1}^{K} {i_{0m}}^2\left(k\right)\sum_{k=1}^{K} {i_{0n}}^2\left(k\right)}} \tag{19}$$

5. FAULT IDENTIFICATION PRINCIPLE OF TRANSIENT INFORMATION FUSION

5.1. Information Fusion Technology

Fault transient information is affected by the nature of the fault and system parameters. Under different fault conditions, the degree of obviousness of transient characteristic information such as power and frequency downstream and upstream of the fault is also different. Therefore, it is crucial to acquire and analyze various transient characteristics following a single-phase ground fault and use information fusion technology to integrate various algorithms. The organic combination makes fault identification robust and improves accuracy. Fig. 7 shows the decision-level fusion structure [22].

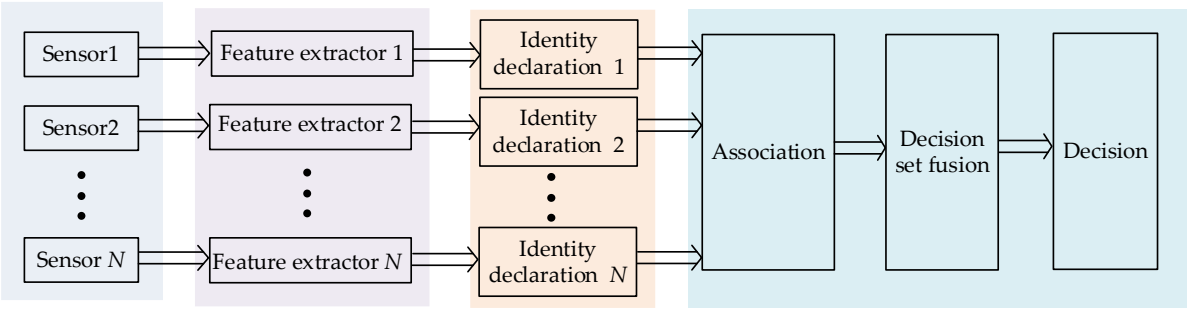

Fig. 7. Decision-level fusion structure.

5.2. Fuzzy Theory and Membership Functions

Fuzzy theory is an important part of current intelligent technology, often applied to deal with complex and uncertain problems. In actual implementations, the main challenge is to establish membership functions correctly.

(1) The output of the fault section identification system shows that a certain section is either a fault section (1) or not a fault section (0), and the judgment result must be taken from {0, 1}. Fuzzy decision-making enhances the flexibility of the absolute membership relationship for fault sections by extending the membership value of each element to the interval [0, 1]. The membership function represents the uncertainty of the fault in each line section, and then fuzzy operation is performed to output the section identification result.

(2) The membership functions of each method differ, implying varying levels of failure probability. These distinctions are harmoniously integrated through fusion calculations. To better accommodate the characteristics of fault section identification, opting for the addition operation is more appropriate. The overall fault decision credibility for a specific line section is determined by summing the product of the membership degree of each method for fault section identification decision and the degree of support of the

method's observation value for the fault positioning decision (fuzzy credibility coefficient).

5.3. Construction of Membership Functions

(1) Membership functions of transient power method

The difference between the transient power direction parameters of the upstream (Q_{n1}) and downstream (Q_{n2}) measurement points is calculated:

$$\Delta Q_n = \left\| Q_{n1} \right| - \left| Q_{n2} \right\| \tag{20}$$

Let ΔQ_{max} represent the maximum value in the array ΔQ_n, the sum of all transient power direction parameter differences on the faulty line is ΔQ_{sum}. The transient power direction parameter method's fault membership function is described as follows:

$$\begin{cases} \mu_p(n) = \Delta Q_n / \Delta Q_{max} \\ \Delta Q_{sum} = \sum_{n=1}^{N} \Delta Q_n \end{cases} \tag{21}$$

According to the analysis in section 2, it can be known that the amplitudes of transient currents at both ends of the fault point are totally different while those at the same ends of the fault point are virtually identical. Thus, the difference of the transient power directions at measurement points at both ends of the fault section is far larger than that of the healthy section. Thus, the weight coefficient membership function of this method is defined as:

$$A_p(n) = \Delta Q_{max} / \Delta Q_{sum} \tag{22}$$

It can be known from Eq. (22), the larger the value of $A_p(n)$, the more probability of a fault occurring in a line section.

(2) Membership functions of characteristic frequency method.

In general, a power distribution network with numerous outgoing lines has a much longer total length upstream of the fault site than the lines downstream of the fault. Thus, compared to the downstream lines, the upstream lines have substantially larger ground capacitance and inductance. The upstream network's main resonant frequency is low and the downstream network's main resonant frequency is high under typical fault situations. The characteristic frequency difference between section n's upstream and downstream is formulated as Eq. (23).

$$\Delta f_n = \left| f_{n1} - f_{n2} \right| \tag{23}$$

where f_{n1} and f_{n2} represent the zero-mode current's main resonant frequency at the upstream and downstream measurement sites. Let Δf_{max} represent the maximum value in array Δf_n, and the sum of all maximum characteristic frequency differences on the fault line is Δf_{sum}, define the fault membership function of the characteristic frequency method as:

$$\begin{cases} \mu_f(n) = \Delta f_n / \Delta f_{max} \\ \Delta f_{sum} = \sum_{n=1}^{N} \Delta f_n \end{cases} \tag{24}$$

There are special circumstances when the fault point is located very close to the busbar and one of the healthy lines is short in length. In such scenarios, there may be a situation where the main resonant frequencies on two sides of the fault location are close to each other. In this case, the reliance on the characteristic frequency method to ascertain the credibility of the fault

section is notably diminished. Therefore, the credibility function of the characteristic frequency method can be determined based on the ratio of the maximum characteristic frequency difference to the sum of maximum characteristic frequency differences on the line. As analyzed in Section 3, the dominant resonant frequencies of transient zero-mode currents in the faulted section differ significantly from those in the healthy section. Besides, the main resonant frequencies of the transient zero-mode currents upstream the fault point are also different from those downstream the fault point. Thus, the difference between the main resonant frequency and the sum of all maximum characteristic frequency differences in the fault line of the fault section is larger than that of the healthy section. The weight coefficient membership function of the characteristic frequency method is defined as:

$$A_f(n) = \Delta f_{max} / \Delta f_{sum} \tag{25}$$

As evident from Eq. (25), the magnitude of $A_f(n)$ is positively correlated with the likelihood of fault occurrence in a given line section.

(3) Membership functions of transient current similarity method.

The maximum value of the current's correlation coefficient at the two measurement points in section n is defined as ρ_n, and the fault membership function of the transient current similarity method is:

$$\mu_s(n) = \begin{cases} 0 \quad (\rho_n \geq 0.8) \\ \frac{4}{3} - \frac{5}{3}\rho_n \quad (0.2 \leq \rho_n < 0.8) \\ 1 \quad (0 \leq \rho_n < 0.2) \end{cases} \tag{26}$$

When the upstream main oscillation frequency and the downstream main oscillation frequency are approximately equal, the correlation coefficient is about 1. In cases where a certain location on the fault line, and the main resonant frequencies of the current on two sides are approximately equal, then the line may be misjudged. Section 4 analysis reveals significant differences in transient zero-mode current waveform similarities between faulted sections and healthy sections. In healthy sections or the sections at the same end in the fault line, the waveform similarities of the transient zero-mode currents are almost equal. However, the waveform similarities of transient zero-mode currents upstream and downstream the fault point are totally different. Thus, the correlation coefficient between the transient zero-mode currents measured at both ends of the fault section can be used to construct the weight coefficient membership function. Let $\rho_{\min}$ represent the minimum value in the array, then the weight coefficient membership function of the current similarity method is:

$$A_s(n) = \begin{cases} 0 \quad (\rho_{\min} \geq 0.8) \\ \frac{4}{3} - \frac{5}{3}\rho_n \quad (0.2 \leq \rho_{\min} < 0.8) \\ 1 \quad (0 \leq \rho_{\min} < 0.2) \end{cases} \tag{27}$$

Equation (27) demonstrates that the fault probability in a line section increases with higher $A_s(n)$ values.

5.4. Multi-Information Fusion Fault Section Identification Method Based on Fuzzy Theory

Calculate the fault membership functions of each criterion corresponding to each section and the weight coefficient membership function. The fault section identification result can be

calculated by Eq. (28).

$$F_n = \frac{A_p\mu_p(n) + A_f\mu_f(n) + A_s\mu_s(n)}{\sum_{n=1}^{N}\left(A_p\mu_p(n) + A_f\mu_f(n) + A_s\mu_s(n)\right)} \tag{28}$$

A fault section identification system is constructed as Fig. 8 after getting the comprehensive criterion of Eq. (28). The system consists of a main station, a substation terminal, and feeder terminal units (FTUs). Data is exchanged between the main station and each terminal unit through switch. Information about zero-mode current is recorded by the FTUs and uploaded to the main station. After then, the data is processed by the main station to identify the problematic area.

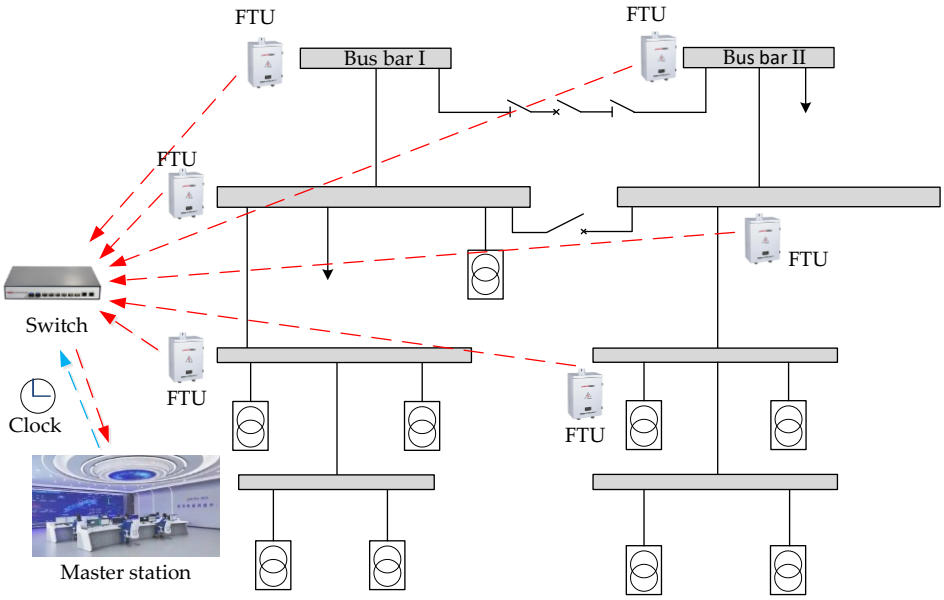

Fig. 8. fault section identification system.

The procedure for a given fault section is as follows:

(1) By analyzing the zero-mode current data from each measuring point and employing the half power frequency cycle data after the fault, one can determine the direction of the transient zero-mode current power for each measuring point using Eq. (9). Subsequently, the correlation coefficient of the zero-sequence current for each section can be calculated using Eq. (19).

(2) Apply the S transformation to each set of transient zero-mode current data in order to generate the corresponding multidimensional complex time-frequency matrix. The modulus time-frequency matrix is then obtained by applying the modulus operation to the matrix. Next, determine the main resonance frequency.

(3) Calculate the fault membership function value sequence of each method for each section and their weight coefficient membership function values and bring them into Eq. (28) to obtain the section where the fault is located.

To evaluate the computational performance of the proposed method, the total time to implement the method is determined. According to the method, the total implementation time includes the time for data measurement and communication and computational time of the algorithm. Although centralized data processing is adopted, the volume of the required data is small and parallel data transmission is used. In addition, the time for data measurement and communication is significantly reduced by employing high-speed data acquisition and

optical-fiber communication, which has been achieved in practice. The computation time of the algorithm consists of two parts: the time for construction of membership functions and that for multi-information fusion. Since there is no iterative calculation in construction of membership functions and multi-information fusion, the total computational time is brief. In simulation, all the computations are conducted in a computer whose processor is Core i5 9300H@2.4 GHz. The time for construction of membership functions is about 30 ms and that for multi-information fusion is about 10 ms. Thus, the computation time of the algorithm is about 40 ms.

6. Simulations

A 35 kV neutral point ungrounded system after a fault was built in PSCAD/EMTDC, and different fault conditions were set for simulation. To confirm the efficacy of the suggested approach, the fault data from the simulation is imported into MATLAB for processing and computation.

6.1. Simulation Model and System Parameters

This model Fig. 9 represents a single-ended radial power grid with four outgoing lines, each utilizing a distributed parameter model. The transformation ratio of the system input transformer is 110/35 kV. The lengths of each outlet line are: 26 km, 30 km, 18 km, 10 km. Figure 9 displays the overhead line's geometric parameter model. The zero-sequence impedance is 0.51664+j1.48516 Ω/km, and the zero-sequence ground admittance is j1.47574326×10^{-6} s/km, the positive sequence impedance is 0.25542+j0.37294 Ω/km, and the positive sequence admittance to ground is j3.0803×10^{-6} s/km. There is a single-phase ground fault occurring in phase A of outlet line 1. A through D are the four current measurement locations along the line. The length of AB section is 10 km, the length of BC section is 10 km, and the length of CD section is 6 km. The measurement points at the head ends of outlet lines 2, 3, and 4 are E, F, and G respectively. In addition, the simulation step size is 1 μs, and the sampling frequency is 10 kHz.

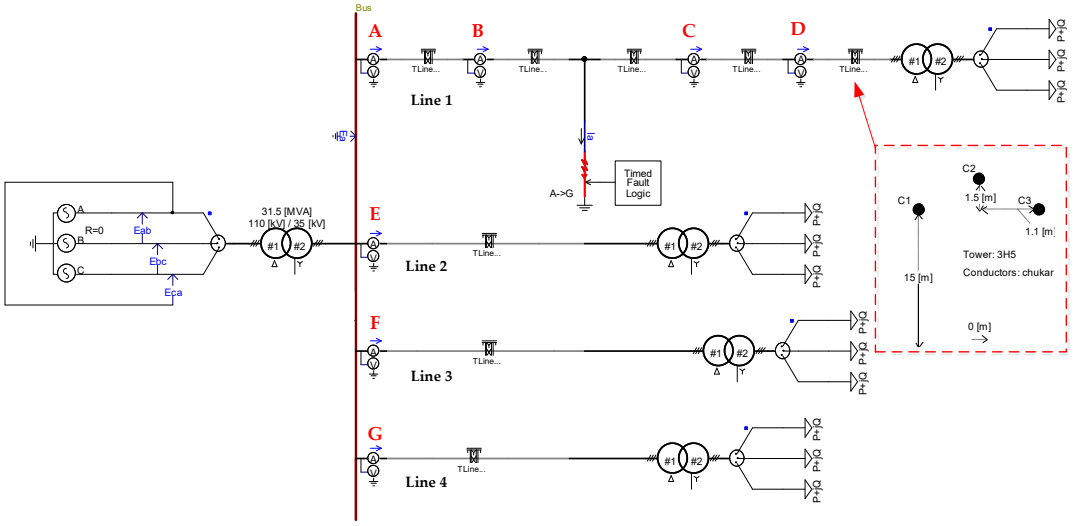

Fig. 9. 35kV distribution network fault simulation model.

6.2. Simulation Result Analysis

In section BC, 15 kilometers from the bus is the location of the fault. The initial phase

angle is 60°, while its resistance measures 10 Ω. The original and transient waveforms of the fault line voltage, as well as its Hilbert transform, are illustrated in Fig. 10. The transient waveforms of the fault's upstream and downstream measurement locations are displayed in Fig. 11. The upstream current (A, B) exhibits an opposite polarity to the downstream current (C, D), which aligns with the theoretical analysis in Section 2. The upstream current shows higher amplitude and lower-frequency oscillations (dominated by system-wide capacitance), while the downstream current reflects localized high-frequency components (due to the smaller equivalent capacitance downstream). This distinction supports the characteristic frequency method's rationale (Section 3). In addition, it can be clearly seen from the waveform similarity that the current on the same side of the fault point has a very high similarity, while the current on both sides has a low similarity.

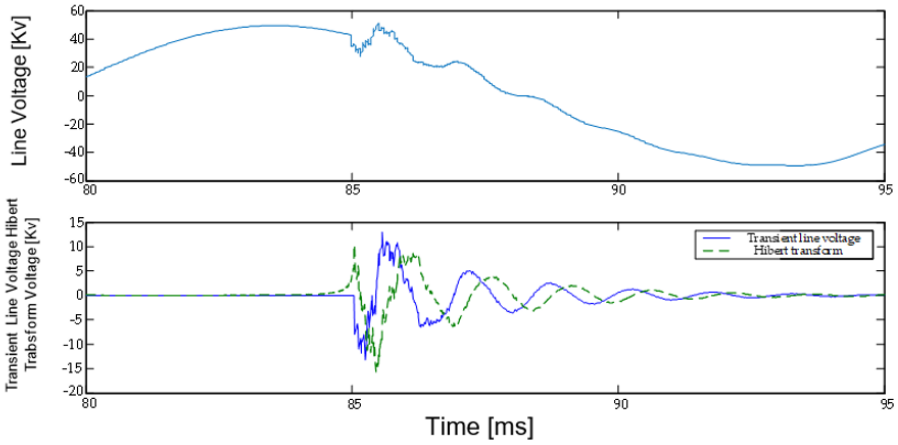

Fig. 10. Line voltage waveform and transient component.

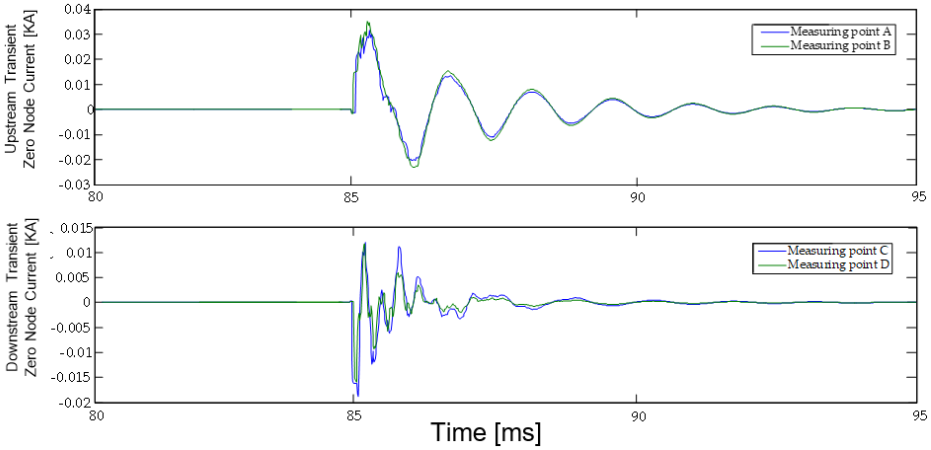

Fig. 11. Transient components of upstream and downstream zero-mode current.

The main resonant frequencies produced via S transform are displayed Fig. 12. Upstream (Left): The dominant resonant frequency is about 700 Hz, consistent with the larger equivalent inductance/capacitance of the upstream network (longer line lengths). Downstream (Right): The dominant frequency shifts to about 3000 Hz, reflecting the smaller equivalent parameters downstream.

The transient power direction parameters, correlation coefficient and main resonant frequency of the zero-mode current of each part are calculated. The fault probability of each section is then determined by computing the fault measurement membership function value and the weight coefficient membership function value for each section. Table 1 shows the simulation data and fault section identification analysis results.

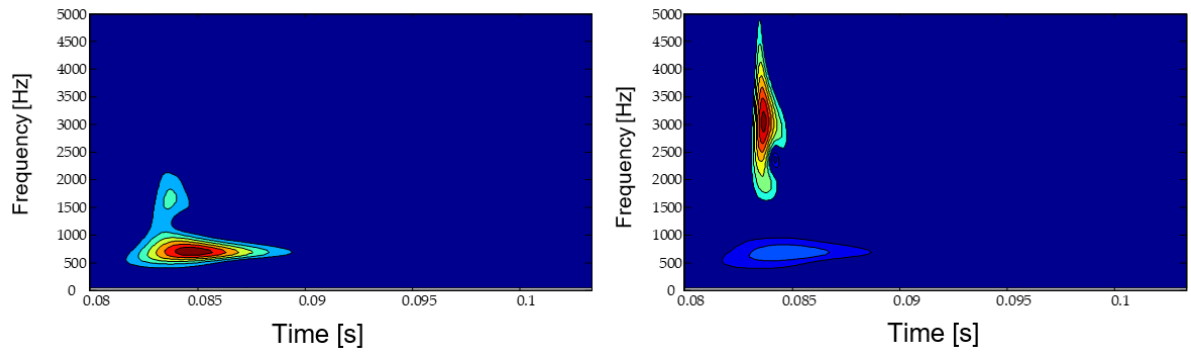

Fig 12. Main resonant frequencies upstream (left) and downstream (right) of the fault location.

Table 1. Simulation data and fault section identification analysis results.

Measuring point		A	B	C	D
Direction parameter		-13922.4	-15643.3	1351.8	588.4
Characteristic frequency		700	700	3000	3000
Section number		AB		BC	CD
Correlation coefficient		0.9855		0.3422	0.8858
Methods	Weight coefficient	Fault membership function value			
Transient power	0.8519	0.1203		1.0000	0.0534
Characteristic frequency	1	0.0000		1.0000	0.0000
Transient current similarity	0.7631	0.0000		0.8453	0.0000
Fault probability of each section		0.0387		**0.9440**	0.0173
Fault section identification result		BC			

The simulation considers the impact of fault resistance, fault phase angle, and fault distance. It establishes several fault scenarios to verify the reliability of the multi-information fusion ground fault location method, which is based on fuzzy decision theory. Table 2 displays the location results under various fault circumstances. The corresponding zero-mode current waveforms for both low and high fault resistances presented in Table 2 are displayed in Fig. 13.

Table 2. Fault section identification results under different fault conditions.

Fault distance [km]	Fault resistance [Ω]	Fault initial phase angle [°]	Fault probability of each section			Section identification results
			Section AB	Section BC	Section CD	
3	10	60	**0.5014**	0.1847	0.3139	AB
		90	**0.4960**	0.1909	0.3131	AB
	100	60	**0.5277**	0.1929	0.2794	AB
		90	**0.5206**	0.1976	0.2818	AB
15	10	60	0.0387	**0.9438**	0.0175	BC
		90	0.0392	**0.9385**	0.0223	BC
	100	60	0.0283	**0.9605**	0.0112	BC
		90	0.0291	**0.9683**	0.0026	BC
23	10	60	0.0501	0.0265	**0.9234**	CD
		90	0.0343	0.0301	**0.9356**	CD
	1000	60	0.0522	0.0259	**0.9219**	CD
		90	0.0411	0.0324	**0.9265**	CD

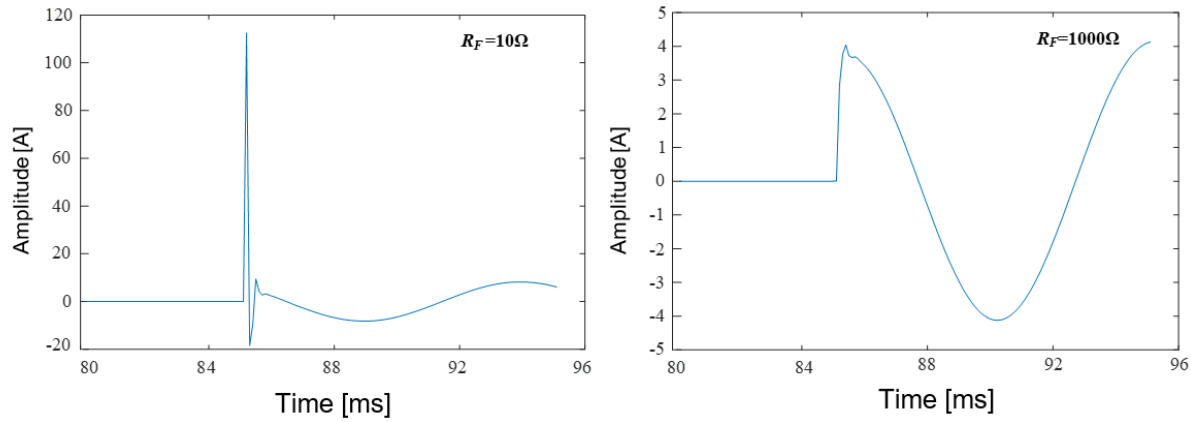

Fig. 13. zero-mode current waveforms for both low and high fault resistances.

Applying the three approaches to different fault scenarios shows considerable differences in the capacity to find the fault section, according to the results. The multi-information fusion single-phase ground fault section identification method, grounded in fuzzy decision theory, achieves effective fusion of the three methods. This approach enables accurate determination of the fault section, unaffected by some factors, such as transition resistance, initial phase angle, and fault distance.

6.3. Simulation Results in Edge Cases

In practice, faults may occur at locations close to measurement points. To validate the effectiveness of the method in these edge cases, fault experiments with various conditions are simulated at locations near measurement points. The detailed information of the fault experiments and fault section detection results is listed in Table 3. In the table, X_A, X_B and X_C represent the fault distances relative to measurement points A, B and C, respectively. It can be observed that the simulated faults are very close to the measurement points (only 0.01 km). Although the faults are set near the measurement points along the feeder, the computed fault probabilities of the fault section are obviously different from those of the healthy sections. Thus, it can be concluded that fault section location results of the proposed method are not affected by faults near measurement points.

Table 3. Fault section location results with faults near measurement points.

Fault location [km]	Fault resistance [Ω]	Fault inception angle [°]	Fault probability of each section			Section identification results
			Section AB	Section BC	Section CD	
X_A=0.01	10	30	**0.2114**	0.0628	0.0211	AB
		90	**0.2371**	0.0675	0.0249	AB
	1000	30	**0.2058**	0.0616	0.0203	AB
		90	**0.2086**	0.0682	0.0225	AB
X_B=0.01	10	30	0.0614	**0.7439**	0.0324	BC
		90	0.0646	**0.7583**	0.0357	BC
	1000	30	0.0605	**0.7244**	0.0311	BC
		90	0.0623	**0.7361**	0.0349	BC
X_C=0.01	10	30	0.0735	0.0482	**0.8591**	CD
		90	0.0762	0.0495	**0.8783**	CD
	1000	30	0.0714	0.0447	**0.8362**	CD
		90	0.0748	0.0463	**0.8457**	CD

6.4. Compare with Other Methods

The transient power direction method [23], the characteristic frequency method [24], the waveform similarity method [25], and the method in this paper are respectively used for fault section identification. All simulations are performed on the same computational platform. Table 4 displays the section identification outcomes of various fault distances and transition resistances.

It is evident that by combining several fault features, the fuzzy decision theory-based fault section identification approach lessens the likelihood of misjudgment. It is least affected by the error data. The algorithm has strong adaptability and there is no blind area. The processing time of these methods is compared based on the same computer (processor is Core i5 9300H@2.4 GHz) used to conduct computations. The fault detection accuracies of these methods are obtained based on results of 100 fault simulations with various fault conditions. The error of each algorithm is also computed according to the fault detection accuracy. It can be seen that the proposed method has the shortest processing time (only about 40 ms). The fault identification accuracy of the proposed method reaches 97% which is the highest among these four algorithms. Thus, the fault detection error of the method is only 3%.

Table 4. Comparison results of several methods.

Methods	Criterions	Blind area	Influence of error data	Processing time	Identification accuracy	Errors
[23]	Transient power direction	Yes	Great	60 ms	93%	7%
[24]	Characteristic frequency	Yes	Medium	70 ms	92%	8%
[25]	Waveform similarity	Yes	Great	50 ms	94%	6%
Proposed Method	Multi-feature fusion	No	Little	40 ms	97%	3%

7. Conclusions

This study examines the differentiation in transient zero-mode feature distribution between fault and healthy sections within the zero-mode network of neutral point ungrounded systems. Additionally, it introduces a novel fault section identification algorithm based on multi-fault criterion fuzzy information fusion. The primary findings are as follows:

(1) The paper analyzes the time-frequency characteristics and distribution of transient line voltage and zero-mode current based on the fault transient equivalent circuit of neutral point ungrounded systems. It establishes section identification criteria using the transient power method, characteristic frequency method, and transient current similarity method. Each method exhibits unique strengths and can complement one another.

(2) It proposes a single-phase grounding fault section identification method based on multi-information fusion using fuzzy decision theory. By leveraging fuzzy theory, the study provides the fault membership function and the criterion weight coefficient membership function for the three methods. The outcomes of each criterion are fused through weighted summation, enhancing the adaptability of single-phase grounding fault section identification.

(3) Simulation results demonstrate that the proposed approach is resilient to fault resistance, fault distance, and fault initial phase angle variations. Compared with existing methods, it offers high accuracy and dependability, effectively eliminating blind areas in fault section identification.

REFERENCES

[1] Z. Jiao, R. Wu, "A New method to improve fault location accuracy in transmission line based on fuzzy multi-sensor data fusion," *IEEE Transactions on Smart Grid*, vol. 10, no. 4, pp. 4211-4220, 2019, doi: 10.1109/TSG.2018.2853678.

[2] F. Conte, F. D'Agostino, B. Gabriele, G. Schiapparelli, F. Silvestro, "Fault detection and localization in active distribution networks using optimally placed phasor measurements units," *IEEE Transactions on Power Systems*, vol. 38, no. 1, pp. 714-727, 2023, doi: 10.1109/TPWRS.2022.3165685.

[3] P. Zhang, L. Kong, R. Liang, B. Xu, N. Peng, "Fault location method for three-core cable using amplitude ratio of shield-grounding wire currents," *IEEE Transactions on Industrial Informatics*, vol. 19, no. 6, pp. 7456-7467, 2023, doi: 10.1109/TII.2022.3194626.

[4] Y. Sun, Q. Chen, D. Xie, "Novel faulted-section location method for active distribution networks of new-type power systems," *Applied Sciences-Basel*, 2023, doi: 10.3390/app13148521.

[5] X. Tong, X. Dong, S. Manzoor, Y. Wang, Z. Zhao, "robust fault location method for transmission lines using PMUs," *IEEE Transactions on Power Delivery*, vol. 38, no. 4, pp. 2338-2347, 2023, doi: 10.1109/TPWRD.2023.3240717.

[6] J. Gao, M. Guo, X. Shao, D. Chen, "Feature - clustering - based Single - line - to - ground fault section location using auto - encoder and fuzzy c - means clustering in resonant grounding distribution systems," *IET Generation, Transmission & Distribution*, vol. 15, no. 5, pp. 938–949, 2020, doi: 10.1049/gtd2.12070.

[7] Y. Jiang, "Data-driven probabilistic fault location of electric power distribution systems incorporating data uncertainties," *IEEE Transactions on Smart Grid*, vol. 12, no. 5, pp. 4522-4534, 2021, doi: 10.1109/TSG.2021.3070550.

[8] E. Maritz, J. Maritz, M. Salehi, "A travelling wave-based fault location strategy using the concepts of metric dimension and vertex covers in a graph," *IEEE Access*, vol. 9, pp. 155815-155825, 2021, doi: 10.1109/ACCESS.2021.3129736.

[9] A. Ossa, C. Orozco-Henao, J. Marin-Quintero, "Master-slave strategy based in artificial intelligence for the fault section estimation in active distribution networks and microgrids," *International journal of electrical power and energy systems*, 2023, doi: 10.1016/j.ijepes.2022.108923.

[10] J. Dang, Y. Yan, R. Jia, X. Wang, H. Wei, "Fast single-phase fault location method based on community graph depth-first traversal for distribution network," *CSEE Journal of Power and Energy Systems*, vol. 9, no. 2, pp. 612-622, 2023, doi: 10.17775/CSEEJPES.2020.04650.

[11] K. Chen, J. Hu, Y. Zhang, Z. Yu, J. He, "Fault location in power distribution systems via deep graph convolutional networks," *IEEE Journal on Selected Areas in Communications*, vol. 38, no. 1, pp. 119-131, 2020, doi: 10.1109/JSAC.2019.2951964.

[12] M. Lakouraj, H. Hosseinpour, H. Livani, M. Benidris, "Waveform measurement unit-based fault location in distribution feeders via short-time matrix pencil method and graph neural network," *IEEE Transactions on Industry Applications*, vol. 59, no. 2, pp. 2661-2670, 2023, doi: 10.1109/TIA.2022.3231586.

[13] Y. Li, X. Wei, J. Lin, "A robust fault location method for active distribution network based on self-adaptive switching function," *International Journal of Electrical Power & Energy Systems*, 2023, doi: 10.1016/j.ijepes.2023.109007.

[14] K. Moloi, N. Ndlela, I. Davidson, "Fault classification and localization scheme for power distribution network," *Applied Sciences*, 2022, doi: 10.3390/app122311903.

[15] P. Zhang et al, "Faulty cable segment identification of low-resistance grounded active distributions via grounding wire current-based approach," *IEEE Transactions on Industrial Informatics*, vol. 20, no. 5, pp. 7708-7718, 2024, doi: 10.1109/TII.2024.3363083.

[16] Y. Xue, X. Chen, H. Song, B. Xu, "Resonance analysis and faulty feeder identification of high-impedance faults in a resonant grounding system," *IEEE Transactions on Power Delivery*, vol. 32, no. 3, pp. 1545-1555, 2017, doi: 10.1109/TPWRD.2016.2641045.

[17] Q. Wang, T. Jin, M. Mohamed, D. Deb, "A novel linear optimization method for section location of single-phase ground faults in neutral noneffectively grounded systems," *IEEE Transactions on Instrumentation and Measurement*, vol. 70, pp. 1-10, 2021, no. 3513410, doi: 10.1109/TIM.2021.3066468.

[18] N. Peng, K. Ye, R. Liang, "Single-phase-to-earth Faulty Feeder Detection in Power Distribution Network Based on Amplitude Ratio of Zero-mode Transients," *IEEE Access*, vol. 7, no. 99, pp. 117678-117691, 2019, doi: 10.1109/ACCESS.2019.2936420.

[19] N. Stipeti, B. Filipovi-Gri, I. Iger, "signal injection for earth-fault localization in unearthed distribution network," *Electric Power Systems Research*, 2023, doi: 10.1016/j.epsr.2023.109249.

[20] L. Tianyou, H. Chaoyi, Z. Yiyong, "the research and demonstration application of high-impedance faults diagnosis approach in small current neutral grounding system," China International Conference on Electricity Distribution, 2018, doi: 10.1109/CICED.2018.8592550.

[21] P. Ray, S. Salkuti, M. Biswal, "Two accurate hybrid islanding detection schemes for distribution network," *Journal of Intelligent & Fuzzy Systems*, vol. 42, no. 2, pp. 755-766, 2022.

[22] Y. Fu, X. Chen, Y. Liu, C. Son, Y. Yang, "Multi-source information fusion fault diagnosis for gearboxes based on SDP and VGG," *Applied Sciences-Basel*, 2022, doi: 10.3390/app13148521.

[23] Luo, X. Liu, X. Yan," Small current ground fault location method based on Hilbert transform," *Journal of Physics Conference Series*, 2019, doi: 10.1088/1742-6596/1176/6/062041.

[24] H. Hasanvand, A. Parastar, B. Arshadi, M. Zamani, A. Bordbar, "A comparison between S-transform and CWT for fault location in combined overhead line and cable distribution networks," Conference on Electrical Power Distribution Networks Conference, 2016, doi: 10.1109/EPDC.2016.7514785.

[25] L. Kong, H. Nian, "Fault detection and location method for mesh-type DC microgrid using pearson correlation coefficient," *IEEE Transactions on Power Delivery*, vol. 36, no. 3, pp. 1428-1439, 2021, doi: 10.1109/TPWRD.2020.3008924.